Journal of Alloys and Compounds 960 (2023) 170647

Contents lists available at ScienceDirect

Journal of Alloys and Compounds

journal homepage: www.elsevier.com/locate/jalcom

Effect of Y_2O_3 addition on the microstructure and mechanical properties of an $Al_{1.8}CoCrCu_{0.5}FeNi$ BCC HEA

Eduardo Reverte [a,*], Clément Keller [b], Monique Calvo-Dahlborg [c], Germán Alcalá [d], Mónica Campos [a], Juan Cornide [a,d]

[a] Department of Materials Science and Engineering, IAAB, Universidad Carlos III de Madrid, Avda. Universidad 30, 28911 Leganés, Spain
[b] Laboratoire Génie de Production, ENIT-INP, Avenue d'Azereix, Tarbes 65000, France
[c] University Rouen Normandie, CNRS, Groupe de Physique des Matériaux UMR 6634, INSA Rouen Normandie, F-76000 Rouen, France
[d] Department of Chemical and Materials Engineering, Faculty of Chemistry, Complutense University of Madrid, Ciudad Universitaria s/n, 28040 Madrid, Spain

ARTICLE INFO

Article history:
Received 8 March 2023
Received in revised form 17 May 2023
Accepted 18 May 2023
Available online 20 May 2023

Keywords:
Powder Metallurgy
High entropy alloy
Microstructure evolution
Spark plasma sintering (SPS)

ABSTRACT

The present study investigated the influence of Y_2O_3 addition by mechanical alloying (MA) on the microstructure evolution of a BCC High Entropy Alloy (HEA). The characterisation and mechanical properties of the alloy were explored using X-ray diffraction, SEM, EBSD, and nano-indentation. The sintered $Al_{1.8}CoCrCu_{0.5}FeNi$ HEA shows a microstructure formed by an ordered BCC phase (Al-rich) and a second disordered BCC (Cr-rich), while a minor FCC (Cu-rich) appears. These BCC phases show a wide morphology evolution from cuboidal and wave-like structures to irregular shapes. The minor FCC phase also adopts several morphologies as the MA is performed. The introduction of oxide reinforcements and microstructure refinement through mechanical alloying yields a change in phase quantification and grain structure. In accordance with the hardness and elastic modulus values from ordered/disordered BCC phases, the disordered BCC shows higher values than the ordered one. The grain size reduction as well as the solid solution strengthening from the microstructure evolution consequence of the MA are shown to be the main contributors to the increase in hardness and elastic modulus in the consolidated samples.

1. Introduction

Since the pioneer works on multiprincipal alloys in 2004 [1], many studies have been devoted to High Entropy Alloys (HEAs). This category of multiprincipal alloys differs from the traditional alloy design, which is related to one or two main elements [1]. In these alloys the presence of five or more principal elements in equi- or near-equimolar ratio, leads to an increase in the configurational entropy (ΔSconfig) [2]. The properties related to the composition of their phases, crystalline structure and microstructure have been widely studied and classified. HEA are found mainly within face-centred cubic (FCC), body-centred cubic (BCC) or FCC+BCC families, and in a few cases, hexagonal closest packed (HCP) [3,4]. They can show a sole crystalline structure, FCC or BCC, for instance [5,6]. However, they are rarely single phase, as their large number of components tend to stabilize several phases with different compositions, but with a similar lattice parameter [7]. In these alloys, the high mixing entropy values between element pairs hinder the formation of brittle intermetallic compounds [8].

Although HEA can have some interesting functional properties, HEA have been mainly explored as a structural material. Several authors have reported high values of hardness [9–13], yielding strengths [14,15], large ductility [16,17], fatigue resistance [18,19] and fracture toughness [20,21]. Other properties such as wear resistance [22], electrochemical resistance [23] and oxidation behaviour [24] have also been studied. In the case of oxidation resistances, some approaches are based on the formation of stable and dense oxide layers on the surface, usually Al/Cr/Si-O, which could protect the material from further oxidation.

Refractory HEAs (RHEAs) appeared after initial studies focused on HEAs formed by 3d transition metals, addressed for high temperature applications. They are composed of refractory elements (mainly Mo, V, Zr, Ta, W and Nb), which usually show single-phase BCC structures [25]. Their strength and hardness values are above FCC HEAs with high temperature strength and creep resistance. These alloys show great potential to compete with Ni-base superalloys. However, they have very high densities (12–13 g/cm^{-3}) with poor elongation leading to fracture at room temperature [26–28], which is critical for industrial service.

* Corresponding author.
E-mail addresses: ereverte@ing.uc3m.es (E. Reverte).

https://doi.org/10.1016/j.jallcom.2023.170647

The search is thus for a suitable high temperature material without refractory elements that maintains strength and hardness values at moderately high temperatures. At the same time, the composition should be optimised accordingly. Several criteria have been evaluated for the prediction HEA, which include parameters like entropy/enthalpy of mixing, differences in atomic radius, lattice distortion, electronegativity or the valence electron concentration (VEC) [29–35]. However, it was concluded that these terms individually cannot produce robust predictions in some cases. This is due to the complexity and strong interaction within alloy elements [36].

One of the approaches followed for predictions is the Hume-Rothery rules considering the number of itinerant electrons per atom (e/a) [37–39]. Using this method, three domains were identified which correlate HEA compositions, structure, and hardness with e/a values and the average radius of elements. The outcome of this method has already resulted in the design of BCC HEAs, such as some variations of the alloy system AlCoCrCuFeNi [40,41]. Moreover, their microstructures and properties have already been either produced from ingot metallurgy (IM) [9,16,22] or powder metallurgy (PM) techniques [23,42]. Taking into account the potential of the AlCoCrCuFeNi family to develop BCC structures, this work is focused on the composition $Al_{1.8}CoCrCu_{0.5}FeNi$. This composition was previously designed using the e/a domains from [37–39], showing a BCC structure [43,44].

In terms of material processing, most HEAs are developed by IM, using either induction or arc melting to mix the components that are usually based on 3d transition metals. As an alternative route, PM is also employed using fully prealloyed powders and further consolidation by either conventional and non-conventional sintering such as Spark Plasma Sintering (SPS) technique or Cold Isostatic Pressing (CIP) [45]. PM also allows several strengthening methods to enhance the alloys' performance. One of these approaches is the particle reinforced HEAs. Several studies have shown results in this direction. Typically, the reinforcements include using SiC particles or oxides such as Al_2O_3 or even Y_2O_3 of different sizes and quantities [46–48]. Therefore, it is of interest to evaluate the strengthening of the $Al_{1.8}CoCrCu_{0.5}FeNi$ while maintaining its BCC structure. Different processing PM routes have been evaluated for the AlCoCrCuFeNi family depending on the starting powder: i) mechanical alloying (MA) of elemental powders with further sintering by techniques like Spark Plasma Sintering (SPS) in [42] ii) mixture of elemental powders combined with vacuum sintering in [44] and iii) prealloyed powder with further sintering by fast-sintering techniques like SPS or Electric Resistance Sintering (ERS) in [43]. Following these procedures, the alloys showed a variety of FCC and BCC structures depending on their compositions. When these alloys exhibit BCC structures, they have low density, reduced cost and a medium to high hardness (slightly below refractory HEAs) [43].

In summary, the processing method combined with the compositions selected determines the final structure and phases of the alloy. In the case of $Al_{1.8}CoCrCu_{0.5}FeNi$ alloy, it has been shown to form BCC structures. However, it is always composed of two BCC phases, disordered BCC and ordered BCC (usually called B2 in the literature) [43,44]. These two phases appear coupled in several morphologies in the literature, such as spherical, cuboidal nano-precipitates or even weave-like [49]. They have been found to be related to the processing method and to the lattice misfit of the alloy, which is closely related to Al in non-refractory BCC HEAs [50,51].

The mechanical properties are derived from these two BCCs and their morphology, which is dependent on the processing route. Therefore, one objective of the present study is to evaluate the microstructure evolution of $Al_{1.8}CoCrCu_{0.5}FeNi$ alloy by powder metallurgy while aiming to particle reinforce it with Y_2O_3 oxides and MA. This composition was originally designed from the e/a approach and domains proposed by Calvo-Dahlborg et al. [18] to obtain a BCC HEA. The influence of particle reinforcement in the alloy was studied, evaluating its phase evolution and crystalline structures. The possible strengthening mechanisms have been discussed based on their microstructural and mechanical properties characterisation.

2. Materials and methods

In this study, $Al_{1.8}CoCrCu_{0.5}FeNi$ has been considered and processed by PM. The HEA prealloyed powder was obtained from pure elements in a lab scale gas atomizer equipped with an induction furnace (Atomising Systems Limited, Sheffield, UK). For the development of the reinforced material, the atomised powder was mechanically alloyed with 0.25 wt% Y_2O_3 particles (from TJ Technologies & Materials Inc.) of 7 µm mean size using high energy milling (planetary mono mill Pulverisette 6, Fritsch, Idar-Oberstein, Germany).

The MA process was composed of two alternative paths: 1) dry MA under a highly pure Ar atmosphere plus short wet MA cycle and 2) wet MA with isopropyl alcohol ($(CH_3)_2CHOH$) as a Process Control Agent (PCA). Both milling routes were made at 300 rpm with an effective milling time of 30.5 h and 45 h respectively. The ball to powder ratio (b:p) was set to 10:1 with 10 mm diameter stainless steel balls.

In the first case of dry plus wet milling, powder particles tend to agglomerate on balls and container walls making them difficult to work with. Therefore, a further 30 min wet milling step in addition to the 30 h dry milling was performed using 200 ml of ethanol as PCA (300 rpm) to disperse the powder particles. Finally, the resulting wet powders were filtered and dried afterwards. This methodology of dry plus wet milling was also successfully applied in HEAs by Moravcik et al. [52]. These wet/dry MA powders were chosen for later consolidation instead of dry only MA powders.

Independently of the state of the initial powder (mechanical alloyed vs plain prealloyed HEA powders), all of them were consolidated via spark plasma sintering (Dr Sinter, SPS-1050CE from SPS Syntex). The consolidation was made in a 30 mm diameter graphite die previously covered with boron nitride to hinder carbon contamination inwards to produce 30 mm samples of 5 mm height. The sintering started from room temperature up to 1100 ºC with a heating rate (H.R.) of 200 ºC/min. The dwell time at 1100 ºC was set to 1 min to avoid further Cu segregation and overall growth of the microstructure. The temperature in all stages was measured with a K type thermocouple placed inside a 6 mm hole in the middle section of the die, close to the powder. The pressure was kept to a steady 50 MPa during the sintering cycle with pulsed current densities around 1.2 kA/cm^2. Table 1 summarises the parameters for the MA and sintering process.

The powders and sintered samples were analysed by XRD, SEM and EBSD (transversal sections for sintered samples). The equipment used for microstructure characterisation was a field emission scanning electron microscope (FEI Teneo FEG-SEM, Hillsboro, OR, USA) equipped with an electron back-scatter diffraction (EBSD) detector and an energy dispersive spectrometer (EDS). The chemical composition and grain size/morphology via backscattered electron diffraction (EBSD) was analysed on sintered samples as well as the precursor powders. Due to the high plastic deformation sustained by the powder particles during milling for reinforced-HEA, large lattice distortion developed and no Kikuchi patterns can be observed in EBSD for that powder. EBSD acquisitions were performed using a step size of 90 nm with a tolerance angle of 2º to determine grain distribution and orientation.

To evaluate the milling process, the crystallite size and microstrain values (calculated by Scherrer method [53] on the peak (110)) were analysed at different time stages of milling by XRD, performed in a Siemens D5000 diffractometer (Siemens, Munich, Germany) with a Cu cathode ray tube (λ = 1.5406, 1.5444 Å). As mentioned by

Table 1
Summary of processing conditions for powders and SPS consolidated material.

Nomenclature			
Feedstock	Gas Atomised	$Al_{1.8}CoCrCu_{0.5}FeNi$	–
Milling Conditions	Wet Milled	$Al_{1.8}CoCrCu_{0.5}FeNi + 0.25Y_2O_3$	300 rpm | milling time 45 h | b:p 10:1
	Dry/wet Milled		300 rpm | milling time 30.5 h | b:p 10:1
Consolidated Materials	Plain HEA	Sintering T (°C) 1100	Dwell 1min H.R. 200°C/min
	MA-HEA		

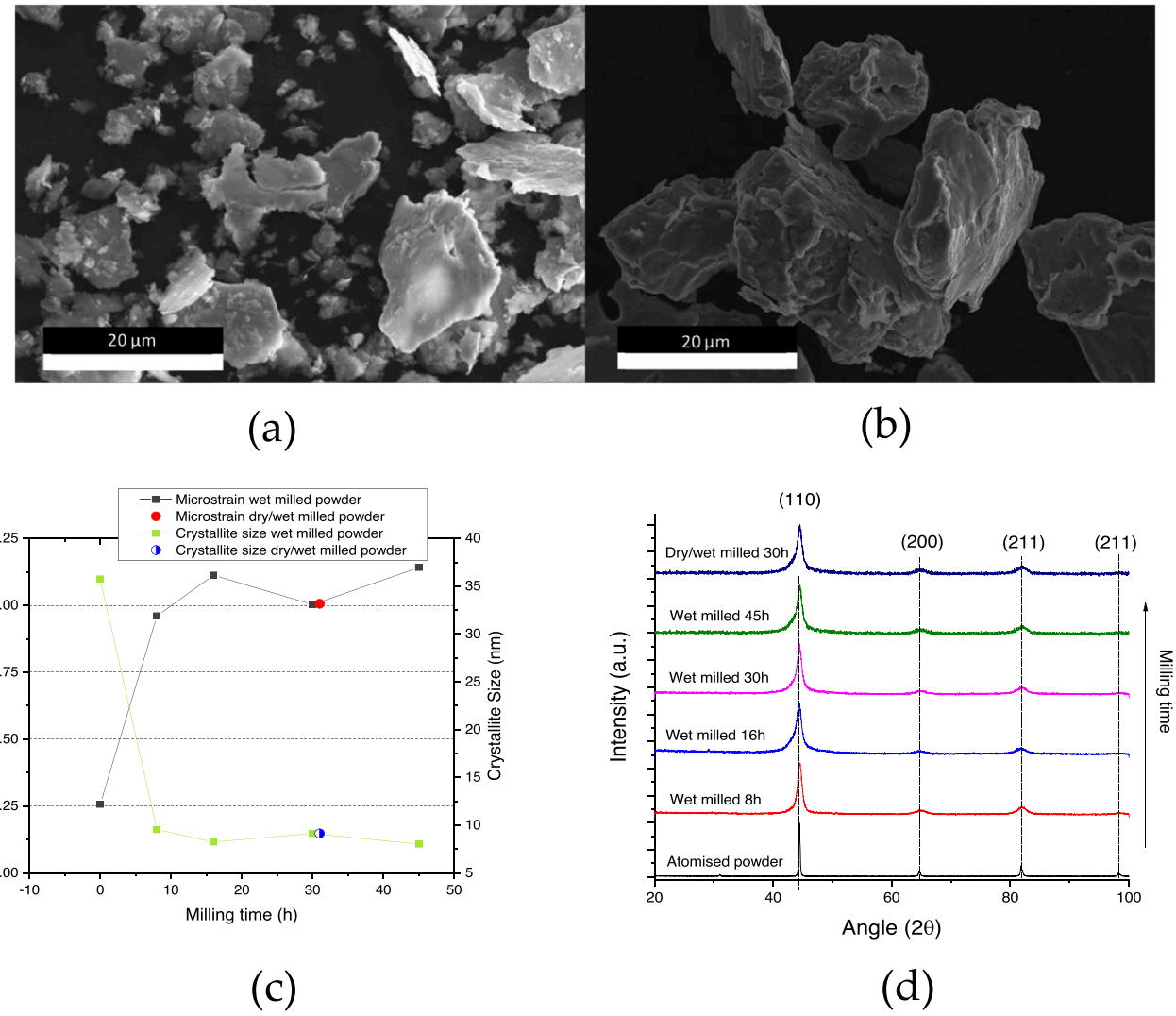

Fig. 1. (a) SE-SEM image of Wet milled powder for 45 h; (b) SE-SEM image of Dry/Wet milled powder for 30 h; (c) Microstrain and Crystallite size evolution versus milling time and (d) XRD patterns of all the specimens at the selected milling times.

Moravcik et al. [52], powder milling using a process control agent can lead to contamination from interstitial elements like Oxygen/Nitrogen or Carbon/Sulphur. To this aim, powder contamination was quantified by solid-state infrared (IR) and thermal conductivity (TC) detectors using a LECO TC-500 and LECO TC CS-200 (both of them from LECO, St Joseph, MI, USA), respectively.

To assess the mechanical properties of the alloys, the hardness tests were performed with two different types of equipment: One for micro-indentations in a ZHVμ hardness tester (Indentec Hardness Testing Machines Limited, Hillsboro, West Midlands, UK) with a peak load of 100 mN; and the second for nano-indentations at a peak load of 500 μN (Hysitron TS 77 Select, Bruker, Massachusetts, USA). The nano-indentations were performed on 11 × 11 μm squares with 0.5 μm of separation between indentations and at a speed of 60 μN/nm.

3. Results and discussion

3.1. Powder consolidation and characterisation: Effect of MA and particle reinforcement on HEA microstructure

The initial atomised powder was milled adding particles of Y_2O_3 to achieve a nominal $Al_{1.8}CoCrCu_{0.5}FeNi$ + 0.25 wt% Y_2O_3 to develop the reinforced alloy. In the high energy milling stage, plastic deformation occurs from the collision between the milling media, steel balls and

Table 2
Chemical compositions of the atomised powder and dry/wet milled powder.

Tag	Al	Fe	Cr	Co	Ni	Cu	Y_2O_3
HEA (at%)[a]	25 ± 3	20 ± 1	14.8 ± 0.7	16 ± 1	15.7 ± 0.3	7.4 ± 0.4	-
Nominal HEA (at%)	28.5	15.8	15.8	15.8	15.8	7.9	-
MA-HEA (wt%)[a]	12.2 ± 0.2	24.1 ± 0.4	15.2 ± 0.3	19.3 ± 0.2	19 ± 0.2	10.2 ± 0.2	-
Nominal MA-HEA (wt%)	15.8	18.2	16.9	19.2	19.1	10.3	0.25

[a] Measured via Energy-dispersive X-ray spectroscopy (EDS)

Table 3
Oxygen and nitrogen chemical analysis of the MA powders.

	Atomised powder		Wet milled powder		Dry+Wet milled powder	
	%Oxygen	%Nitrogen	%Oxygen	%Nitrogen	%Oxygen	%Nitrogen
Total:	0.052	0.015	0.148	0.002	0.246	0.016
% Y_2O_3:			0.053		0.053	
% Ex.O:			0.095		0.193	
% Ex.O*:			0.043		0.141	

Ex.O = Total O content - $\frac{48}{226}$ Y_2O_3 content (wt%)
Ex.O* = Total O content - $\frac{48}{226}$ Y_2O_3 content (wt%) - O content (wt%) in atomised powder

powder. The severe transfer of mechanical energy to the powder causes its fracture and cold-welding, conditioning the microstructure and properties of the final material. Regarding the particle size and according to some previous studies in the literature, powder fracture and cold-welding effects are balanced during the progression of milling, [54,55]. However, when wet milling was performed in this study, powder fracture prevailed over cold-welding even for long periods, resulting in an elongated and flake-like powder (see Fig. 1-a). In contrast, when the milling is performed under dry conditions, cold-welding predominates, sticking the powder, vial and balls together, resulting in low efficiency. However, if both routes are mixed, first a dry stage followed by a second wet milling, the powder reaches an irregular shape more suitable for consolidation in SPS (see Fig. 1-b). This was the powder selected for subsequent sintering.

Related to the solid solution formation, atom diffusion does not significantly affect the inherent arbitrary positions of atoms due to their sluggish diffusion. However, previous studies have shown that copper tends to segregate [44]. As the ΔH_{mix} of unlike pairs become the dominant factor over ΔS_{mix} it promotes the segregation [43], which may also occur during the milling process. Plastic strain and residual stress generated in the powder should relax due to heat in the SPS consolidation resulting in broader copper segregation than in milling. Moreover, other studies have shown that minor copper segregation is observed even in gas atomised powders [43,44].

In Fig. 1-c, the microstrain and the size of coherently scattering domains evolution as a function of milling time are represented. These measurements from different milling strategies (i.e., dry or wet/dry) were obtained from XRD patterns in Fig. 1-d. Once a critical level reaches a plateau, both parameters stabilize in a steady state even with increasing milling times. It is possible to observe that crystalline domains are rapidly stable after 8 h, with an average size of 8.7 nm, while the microstrain reaches a stable value of around 1.05% close to two hours later. When milling time is increased, there is a decrease in the size of the crystallites, indicated by the peak width enlargement from XRD (Fig. 1-d).

The microstrain achieved during the high energy milling (≈1.05%) will determine the consolidated grain size distribution [56]. Furthermore, the balance between dislocation densities due to cold work in MA and thermal recrystallization during SPS consolidation will also establish the minimum average grain size [56].

The nominal and chemical composition of the atomized HEA together with the Dry+Wet milled powder is shown in Table 2. They

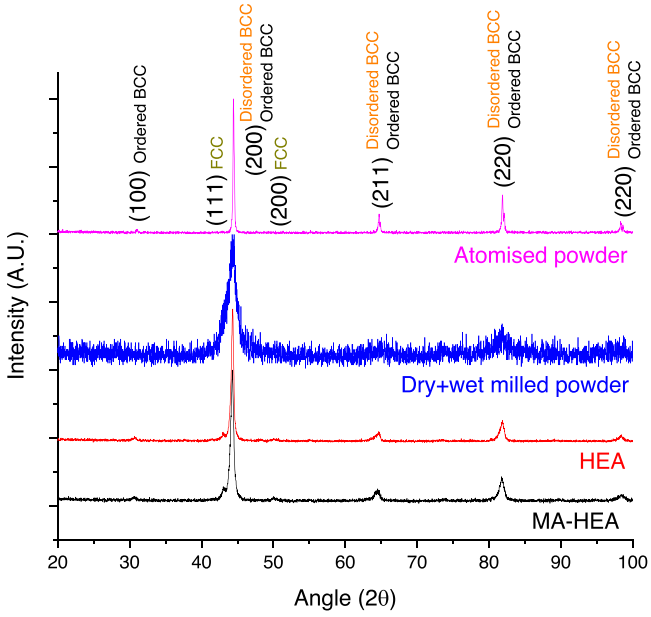

Fig. 2. XRD patterns and comparison between HEA powders (atomised and milled) and consolidated samples (HEA and MA-HEA).

show overall similarities between nominal and experimental data. Foreseeing the formation of undesired oxides and nitrides due to potential contamination arising from the atomisation process, as well as the addition of a process control agent, the interstitial content in the alloy was measured. In the case of other contamination like Fe or Cr from the vials and balls during milling, they could be considered non-relevant contamination as the compositions usually vary from the nominal values.

Aside from interstitial contamination, the literature regarding ODS steels has shown the importance of evaluating and controlling the excess oxygen contents (Ex.O). This parameter is obtained by subtracting the oxygen content from the Y_2O_3 compound from the total O in the alloy. Moreover, a second excess oxygen parameter (Ex.O*) has been calculated which also considers the oxygen content measured in atomised HEA powders. These values summarise the enrichment of oxygen in the milled powder (see Table 3).

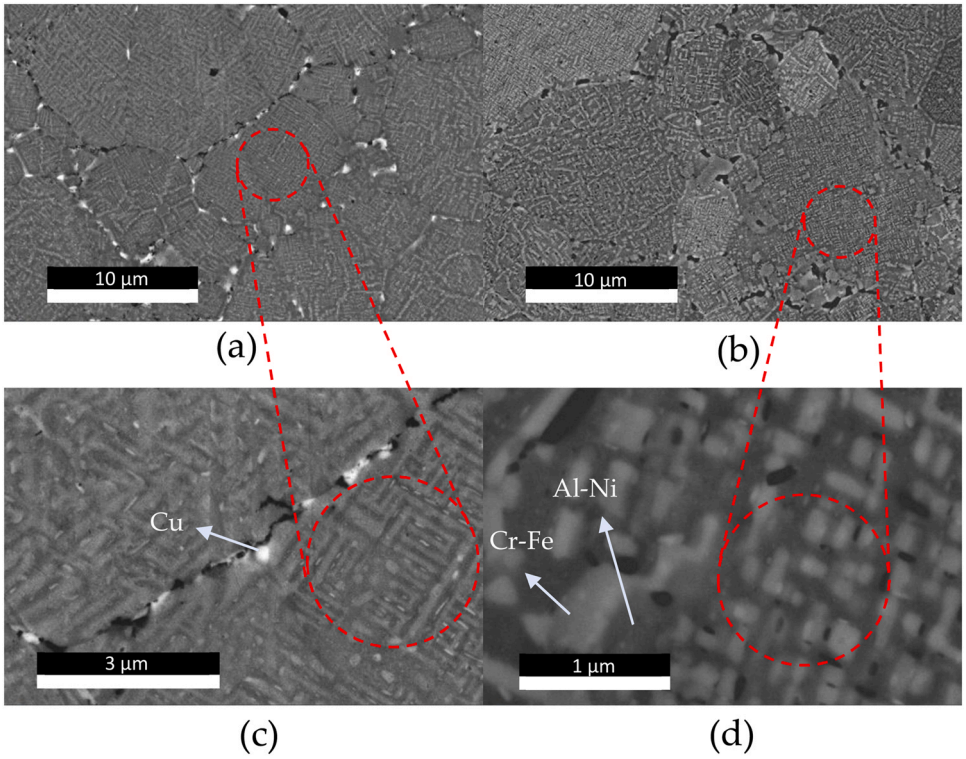

Fig. 3. BSE-SEM images of Plain HEA.

Table 4
Chemical compositions (at%) of phases detected on Plain HEA.

Phase	Al	Cr	Fe	Co	Ni	Cu
Cr-Fe-rich phase "Disordered BCC"	22.3	16.9	22.4	15.5	14.6	8.1
Al-Ni-rich phase "Ordered BCC"	26.7	10.6	19.1	17	18.4	7.9
Cu-rich phase "FCC"	14.2	10.5	11.2	6.6	5.7	51.8

Measured via Energy-dispersive X-ray spectroscopy (EDS)

Indeed, the Ex.O produced in the alloys can drastically improve the microstructure and the high-temperature performance of alloys. Raja Rao et al. [48] studied the strengthening of an AlCoCrFeNi HEA with different oxide weight percentages (ranging from 0 to 3 wt% Y_2O_3). This study showed that Y_2O_3 offers a beneficial effect on the mechanical properties of HEA. However, Ohtsuka et al. [57] concluded that merely increasing the particle addition cannot improve properties such as high-temperature strength. These ideas focus on optimising the right proportion of Ex.O available in the HEA instead of adding large quantities of particle oxides. According to Ohtsuka et al. [57,58], a minimum amount of Ex.O required in their ODS steels is about 0.1 wt%, a value reached in the dry/wet specimens [59].

Aluminium has a FCC crystalline structure. However it is found to induce the formation of BCC structures in HEA. This leads to higher hardness and yield strength [9,49,51,60,61] than FCC alloys. Hence, Al-Transition metals HEAs, such as the one used in this study, generally exhibit BCC structures as Al concentration increases [62]. They are usually composed of two phases, an ordered BCC enriched in Al-Ni and a disordered BCC enriched in Cr-Fe. The ordered BCC precipitates are arranged in spherical, cuboidal nano-precipitates and even weave-like morphologies within the BCC disordered matrix, according to the literature [49,50]. Recent studies on these three microstructures have shown that their formation is affected by the lattice misfit, which is affected by Al content. Moreover, the anisotropy difference of Young's modulus between the two BCC phases has also been proven to affect their morphologies. Both BCCs have shown exchangeable arrangement as either precipitate or matrix. It is of interest that cuboidal and coherent precipitation in the matrix exhibits much higher thermal stability than the weave-like morphology that results in an embrittlement of the alloy [49,50].

Fig. 2 shows that in XRD diffractograms from powder and consolidated samples the BCC structure is predominant. However, a more detailed analysis reveals that the microstructure consists of two BCCs, ordered and disordered, with the combined intensity of both indistinguishable peaks. This feature is in agreement with the literature but further analysis with advanced techniques is needed to correctly distinguish both phases [49]. Nevertheless, SEM analysis of the consolidated HEA using backscattered electrons (see Fig. 3) clearly illustrates these two BCC phases. Both phases adopt different morphologies, ranging from cuboidal-like nano-precipitates to weave-like morphologies (marked in a red circle in Fig. 3-c). This arrangement can be attributed to lattice misfit between ordered and disordered BCCs [49]. The compositional analysis is shown in Table 4. The cuboidal precipitates appear enriched in Cr-Fe (disordered BCC) while the matrix is enriched in Al-Ni (ordered BCC). Moreover, a third minor phase enriched in Cu (FCC) was also observed in the microstructure. Finally, Fig. 4 shows a chemical map of a HEA sample with a Cr carbide. These minor contaminations have appeared multiple times in different processing routes in the literature [43,44].

Fig. 5-a and 5-b show the microstructure of MA-HEA, obtained after the consolidation of the dry/wet milled powder. The most noticeable difference compared to the previous samples is the white phase dispersed along the microstructure. These precipitates are a Cu-rich phase whose composition can be seen in Table 5. Moreover, the oxides introduced in the MA are not visible. This suggests that they are mixed within the microstructure. The influence of these oxides should not be relevant to either BCC formations, either cuboidal or weave-like. In Ni-based superalloys, some oxides formers such as Ti or Al favour the formation of γ' phase [63]. In contrast, Y or Y_2O_3 do not interfere with BCC phase formations in HEA.

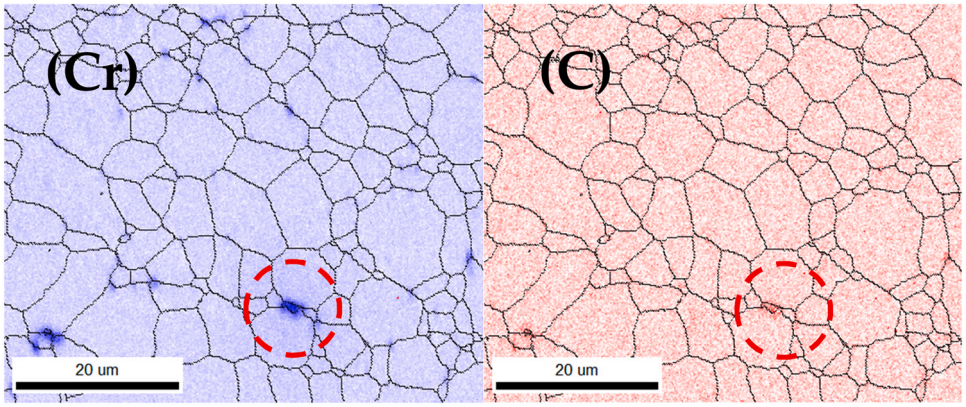

Fig. 4. Chemical compositions detail of carbide in HEA sample.

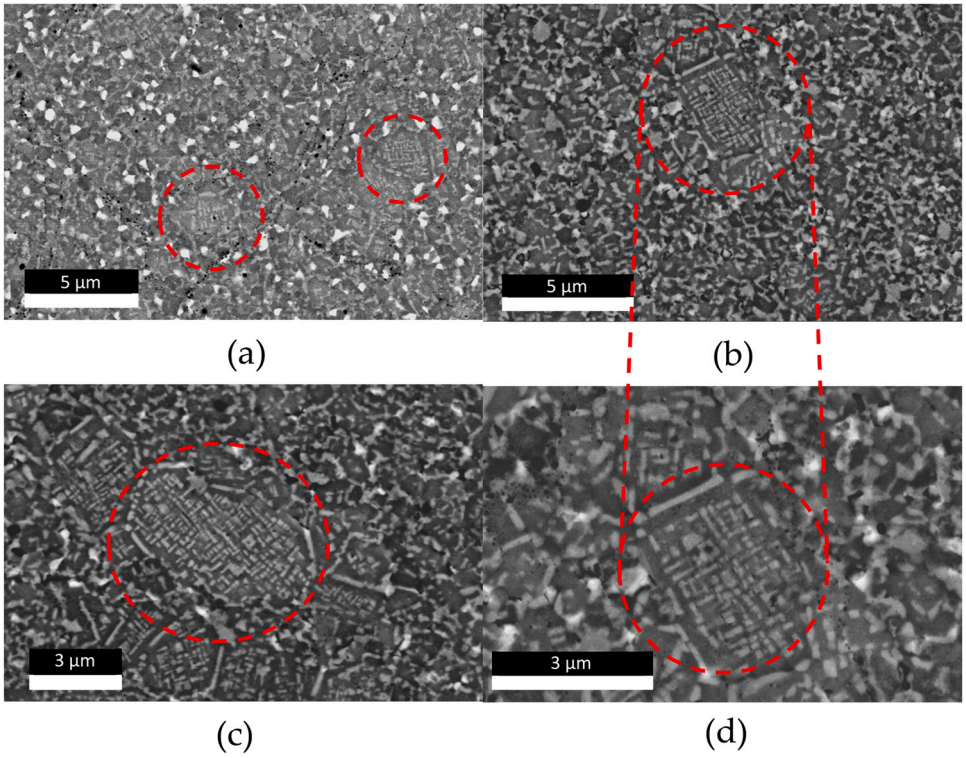

Fig. 5. BSE-SEM images of MA-HEA sample.

Table 5
Chemical compositions (at%) of phases detected on MA-HEA samples.

Phase	Al	Cr	Fe	Co	Ni	Cu
Cr-Fe-rich phase "Disordered BCC"	20.9	18.7	24.1	15.1	13.9	7.1
Al-Ni-rich phase "Ordered BCC"	25.4	12	20	16.9	18.3	7.2
Cu-rich phase "FCC"	17.0	12.5	15.3	8.8	7.9	38.3

Measured via Energy-dispersive X-ray spectroscopy (EDS)

From an image analysis using ImageJ software and colour contrast, this Cu-rich phase occupies about 4–5% of the microstructure. Fig. 5-c shows the presence of two phases randomly distributed within the microstructure. The first phase is visible as a dark matrix, while the second phase appears as cuboidal precipitates similar to those found previously in plain HEA (circled in red). However, these cuboidal morphologies only appear in some regions. This structure may be the consequence of an uneven recrystallization of less deformed particles from the milling stage. As a result, the alloys developed a heterogeneous microstructure.

The microstructures of both processed HEAs are different with complex BCC phases and cuboidal and weave-like morphologies. A closer observation of the two microstructures is represented in Fig. 6 with an image quantification of a reduced section. From image analysis using ImageJ software, the more refined microstructure of the MA HEA sample has decreased the amount of disordered BCC developed in the ordered-BCC matrix from 50% to 30%.

To analyse crystallographic aspects of the HEA evolution through production processes, EBSD observations were carried out on atomised powder, plain HEA and MA-HEA samples (Figs. 7-a, 7-b and 7-c). In the

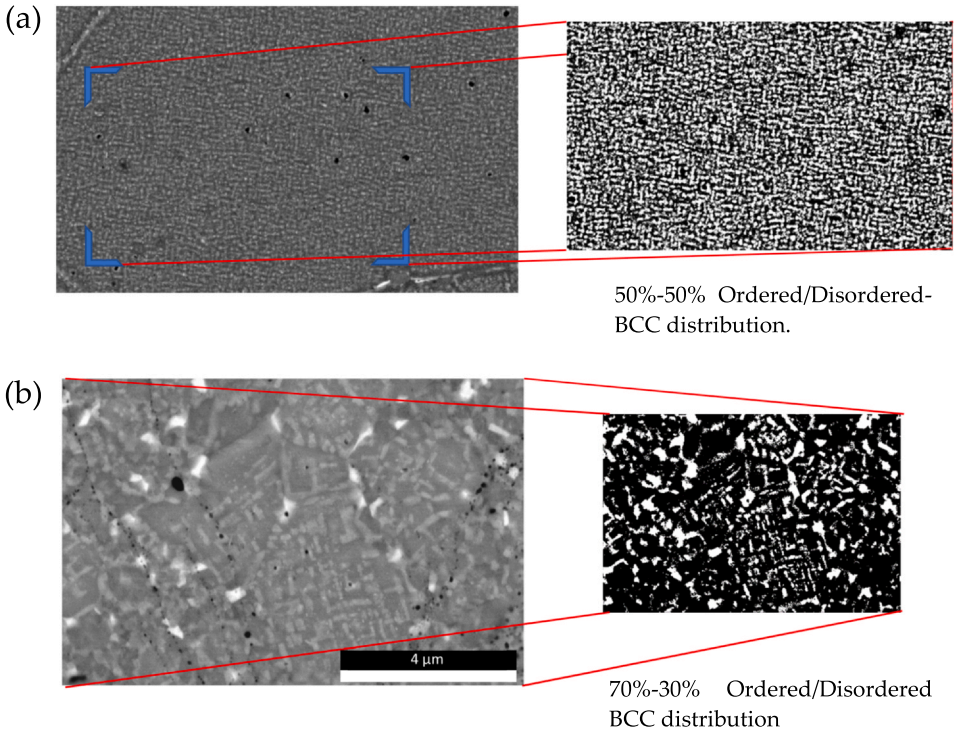

Fig. 6. SEM based BCCs distribution quantification in (a) HEA and (b) MA-HEA microstructure.

case of the milled powder, it could not be observed due to the severe crystallographic strain and plastic deformation from the process.

For the atomised HEA powder (Fig. 7-a), the grain orientation map shows grains with smaller sizes than the average particle ones (D50 = 35.6 µm), suggesting polycrystalline powder particles. Intragranular misorientations are also observed in this image showing the existence of sub-grains and Low Angle Grain Boundaries (LAGBs). These boundaries were considered within rotation angles changes of 5° to 15°. This feature is confirmed by the Kernel Average Misorientation map (KAM) combined with LAGBs (green boundaries) that shows internal sub-grain structures restricted by LAGB. This observation implies that the starting HEA powder has a relatively high value of residual stress developed from the gas atomisation process.

Focusing on sintered HEA samples, the grain orientation maps show well-defined grain structures based on the BCC phase for both sintered samples without intragranular misorientations suggesting a full recrystallization process during sintering. This feature is also confirmed by the KAM maps where large KAM values are always associated with grain boundaries. Some FCC phase (less than 1% in volume fraction) is also observed for these samples. The pole figures do not prompt any preferential grain orientations (maximal density poles of about 2).

A broad grain size distribution is observed focusing on the average grain size, which is 3.7 ± 2.8 µm for the plain HEA versus 0.47 ± 0.43 µm for the MA-HEA. This reveals reduced grain growth during the sintering process, probably linked to the lower scattering domain size produced from the milling stage. This has also been observed for stainless steels produced by similar PM routes [64].

3.2. Mechanical properties and strengthening mechanism discussion

The mechanical properties in alloys depend on multiple factors and different phenomena such as grain size, order, solid solution and dislocation density. To study the influence of different strengthening mechanisms on HEAs, Ganji et al. [65] and Sriharitha et al. [66] evaluated some alloys from the $Al_xCoCrCuFeNi$ family. They observed that small variations in the composition changed the microstructure completely, yielding to a dual phase FCC and an ordered BCC (referred to as B2 in this study). Compared to the alloy $Al_{1.8}CoCrCu_{0.5}FeNi$, the influence on the mechanical properties of dissimilar phases like FCC and BCC will be lower.

The microhardness values of Plain HEA and MA-HEA are 579 ± 37 $HV_{0.01}$ (5.67 GPa) and 614 ± 29 $HV_{0.01}$ (6.02 GPa), from at least 10 indentations respectively. The MA-HEA sample shows an increase in hardness that could be related to different contributions. First of all, the Hall-Petch strengthening or grain size dependent strengthening "σ_{gss}" (Eq. 1).

$$\sigma_{gss} \approx kd^{-1/2} \quad (1)$$

This parameter depends on an empirical coefficient "k". According to different publications on HEAs, several "k" values have been used, varying from 0.677 MPa $m^{1/2}$ [67,68] to 0.27–0.33 MPa $m^{1/2}$ [65,66]. However, the most important factor is the grain size "d" which changes following a reciprocal function ($y = 1/x^{1/2}$, with "y" being the grain size strengthening and "x" the grain size value). Therefore, σ_{gss} rapidly increases with the reduction of the mean grain size. The MA-HEA shows a smaller average grain size of about 400 nm in diameter, compared to the 3 µm from the standard HEA. Therefore, it can be assumed that the MA-HEA sample underwent strengthening produced by grain size refinement of about 36% following Eq. (1).

Another strengthening mechanism is dislocation hardening or "Taylor hardening", which develops from the crossing of dislocations during deformation. In the case of HEAs, Edalati et al. [69] performed a plastic deformation study where the deformation mechanisms of FCC and BCC HEAs were evaluated. FCC phases with low stacking fault energy form nano-twins and stacking faults that expand the lattice structure. However, the BCC's main mechanism is based on dislocation accumulations over strain while the lattice is contracted. The present alloy is mainly formed from BCC structures and therefore dislocation accumulations should be considered. The Taylor strengthening is represented as follows (Eq. 2) [65].

$$\sigma_{TH} \approx M\alpha Gb\rho^{1/2} \quad (2)$$

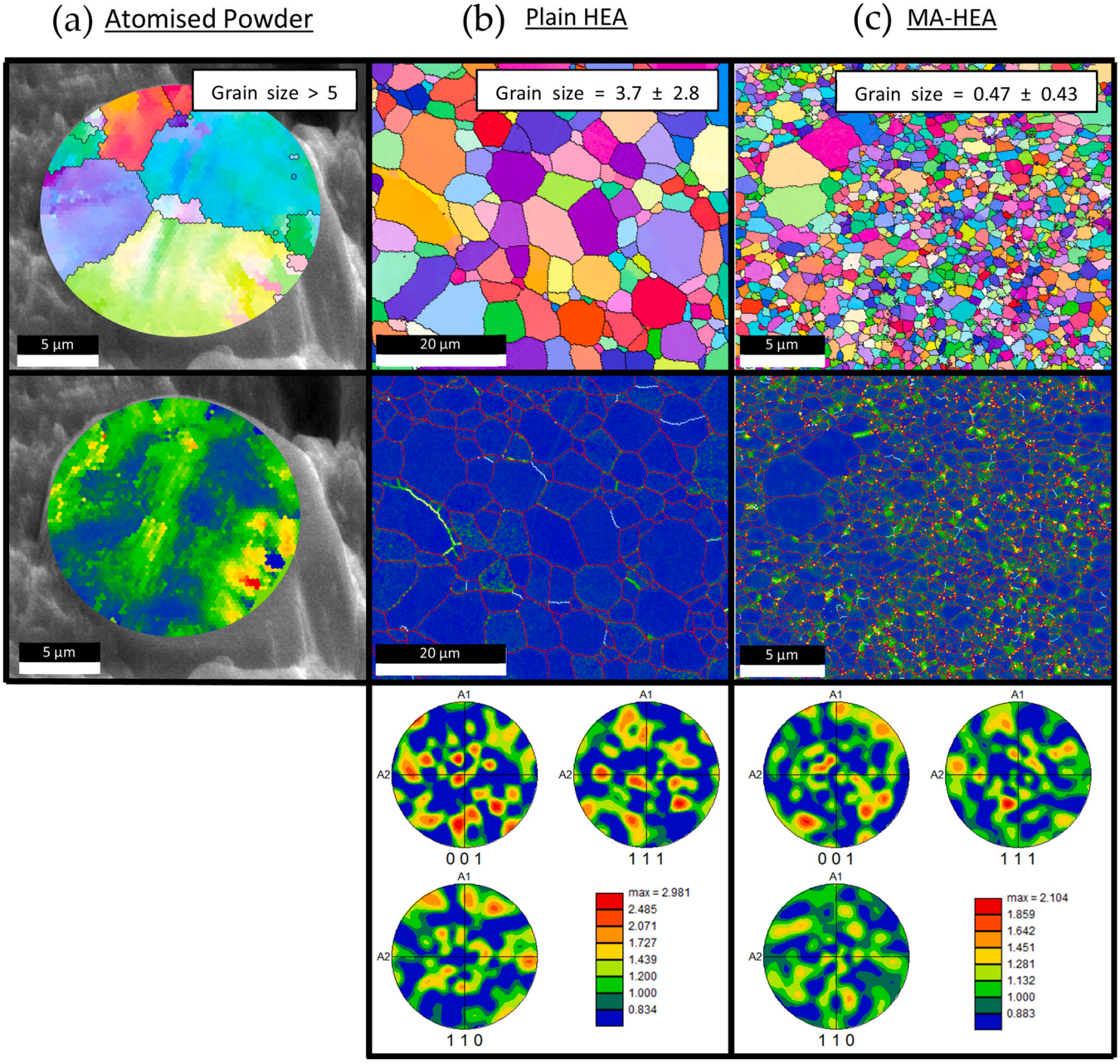

Fig. 7. Inverse pole figures (IPF), KAM + High/Low angle grain boundaries (HAGBs/LAGBs) and Pole figures (PF) via EBSD for (a) atomised powder (b) Plain HEA sample and (c) MA-HEA sample.

The strengthening is composed of M as the Taylor factor that varies from the type of structure, α is a correction factor dependent on each material, G is the shear modulus, b is the Burgers vector and ρ is the dislocation density, which can be assumed as in Eq. (3) from [65].

$$\rho \approx \frac{2\sqrt{3}}{d} \frac{\varepsilon}{b} \tag{3}$$

In this equation, ε is considered the microstrain (calculated by Scherrer method [53] as previous analysis in particles characterisation), taking into account the difference in grain size and microstrain values calculated from HEA and MA-HEA samples. The Taylor strengthening of MA-HEA triples the one approximated from HEA samples. The Kernel average misorientation maps in Fig. 7 confirm this with some regions where dislocation density is high. Therefore, this results in an increase of hardness values from the Taylor hardening component in the MA-HEA.

Regarding other strengthening contributors, there are two more plausible factors which are order strengthening (σ_0) and solid solution strengthening (σ_{ss}). In the first case, the order contribution stands for the lattice frictional stress offered by the lattice in the dislocation motion. The two-phase interaction (ordered/disordered BCC) and lattice complexity contribute to increasing the frictional stress produced by the lattice for mobile dislocations, and hence the σ_0 contribution. At present, no frictional stress data can be found in the literature due to the novelty of HEAs. Some authors have calculated estimations by the rule of mixtures [65,66]. This suggests that this component depends on the composition and not on the processing method.

Other contributions to evaluate would be the solid solution strengthening mechanism and the precipitation hardening produced from the oxide introduced. The solid solution strengthening involves both BCC phases, as they are essentially solid solutions with

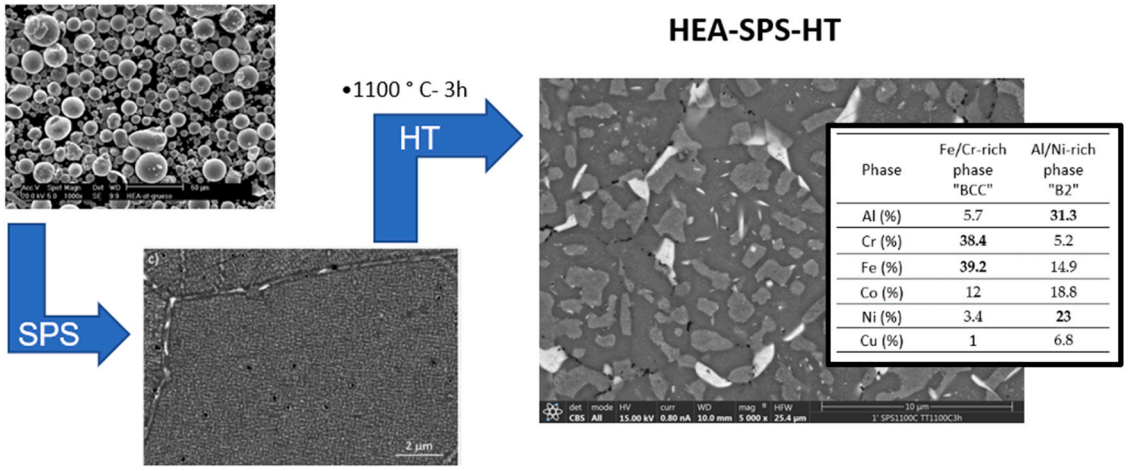

Fig. 8. Processing route for the heat-treated SPS HEA.

Table 6
Hardness and reduced modulus measured via nano-indentation in the different HEA specimens in this study.

Material		H (GPa)	E_r (GPa)
Powders	Plain HEA Atomized Powder	6.3 ± 1.5	41 ± 12
	Dry/Wet Milled Powder	9.6 ± 1.5	74 ± 13
Consolidated Samples	HEA	9 ± 2	161 ± 47
	MA-HEA	9.7 ± 0.8	201 ± 13
	HEA + HT	8.4 ± 1.1	207 ± 13

dissimilar element compositions. As dislocations progress elastically through the lattice, they interact with the distortions created by the substitutional solutes. This interaction in cubic structures distorts the crystal both geometrically (atom size mismatch) and chemically (electrical and bonding variations). However, these norms are not applicable to HEAs and the concept of solute/solvent does not exist for these materials. Some studies have attempted to extend conventional models of solute strengthening to HEA [70–72]. An example of this is the model based on an average effective medium by atomistic simulations, which has successfully been able to predict

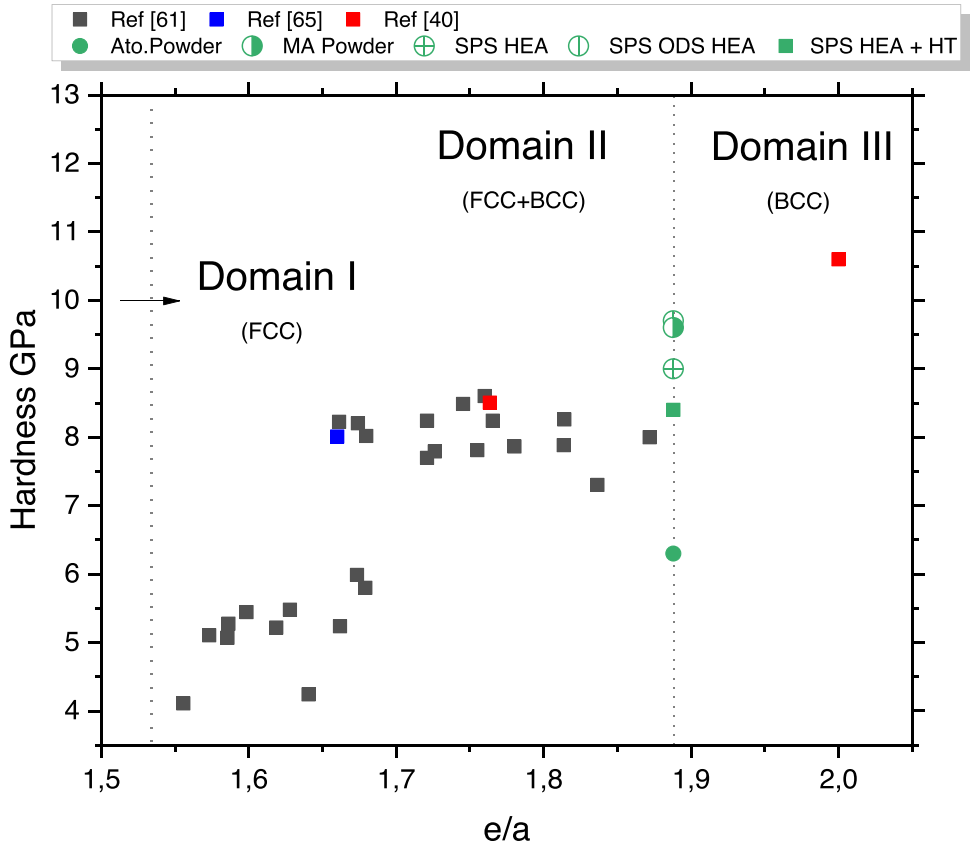

Fig. 9. Hardness by nano-indentation from the current study compared to various literature HEAs, $Al_xCoCrFeNi$ [61], AlCoCrCuFeNi [65]and $Al_xCoCrCuFeNi$ [40].

the strength of FCC HEAs with experimental results [73]. For BCC HEAs, the most accepted deformation mechanism is kink-pair nucleation for dislocations motion, although it is still unknown if the solid solution promotes or hinders the dislocation motion. Baruffi et al. [74]. studied two recent theories based on the wavering behaviour of dislocations in random mediums. They suggest that in highly concentrated alloys, the strength is dominated by edge dislocations instead of screw dislocations. This behaviour is key to understanding the high temperature properties of BCC HEAs. Moreover, the shear modulus of the alloy, the elastic modulus mismatch and the atomic size mismatch are the dominant factors affecting the strength of the alloy [74–76].

The precipitation strengthening also can play a leading role in hardening the alloy. Raja Rao et al. [48] showed that even small additions of 1 wt% of Y_2O_3 can increase the hardness of a mechanical alloyed HEA by 34%. These precipitates could not be seen by regular SEM observations. Therefore, this suggests that these oxides are dispersed in submicron regions in the microstructure.

To analyse the hardness influence of both BCC phases in solid solutions, nano-indentation tests were performed on the microstructure of the alloys at a peak load of 500 μN. It is important to note that cuboidal precipitates are usually coherent in these types of alloys and their strengthening contributions should not be very relevant [49].

It was not possible to clearly discern the hardness of each individual phase due to the small size of the microstructure. For this purpose, the plain HEA was heat treated at 1100ºC for 3 h to increase the grain and phase sizes developed in the microstructure. The nano-hardness tests were performed in the transversal section of the sample after mirror polishing and cleaning the surface for reliable data acquisition. An illustration of the heat treatment performed is shown in Fig. 8, with an SEM micrograph as an example of the obtained microstructure. Both phases are clearly visible, and they were analysed compositionally and structurally to be the same two ordered/disordered BCC phases and with a similar composition as the non-heat-treated HEA. The brighter phases correspond to the FCC Cu-rich phase also observed without heat treatment.

The average hardness and reduced modulus values extracted from the nano-indentation in all HEA samples are summarised in Table 6. The reduced elastic modulus act as a correction between the intender tip and sample elastic strains to accurately measure hardness values. The lowest hardness value corresponds to the atomised powder, and it greatly increases after the milling process, as observed from the Dry/Wet milled powder. Once both powders are sintered, hardness and elastic modulus also increase due to the consolidation process and strengthening mechanisms. On the contrary, the hardness of the heat-treated sample is lower than the consolidated HEA sample, as expected due to stress relaxation, solid state diffusion, and grain size growth. It is important to note that the low elastic modulus obtained in the powder particles is expected to be lower in spherical particles [77]. In addition, the measurements may suffer from substrate interference.

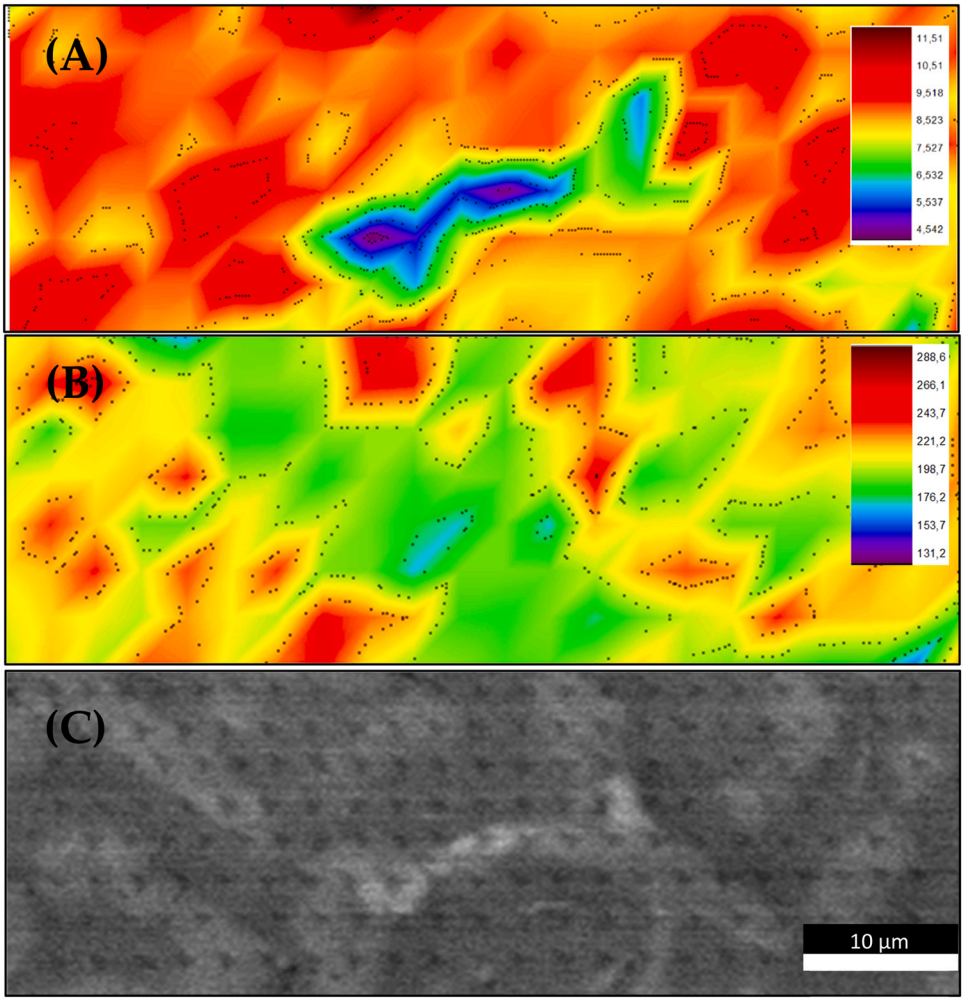

Fig. 10. Contour mapping from the nano-indentation performed on the heat-treated HEA sample (a) Hardness (b) Reduced Elastic Modulus and (c) BSE-SEM image after indentations.

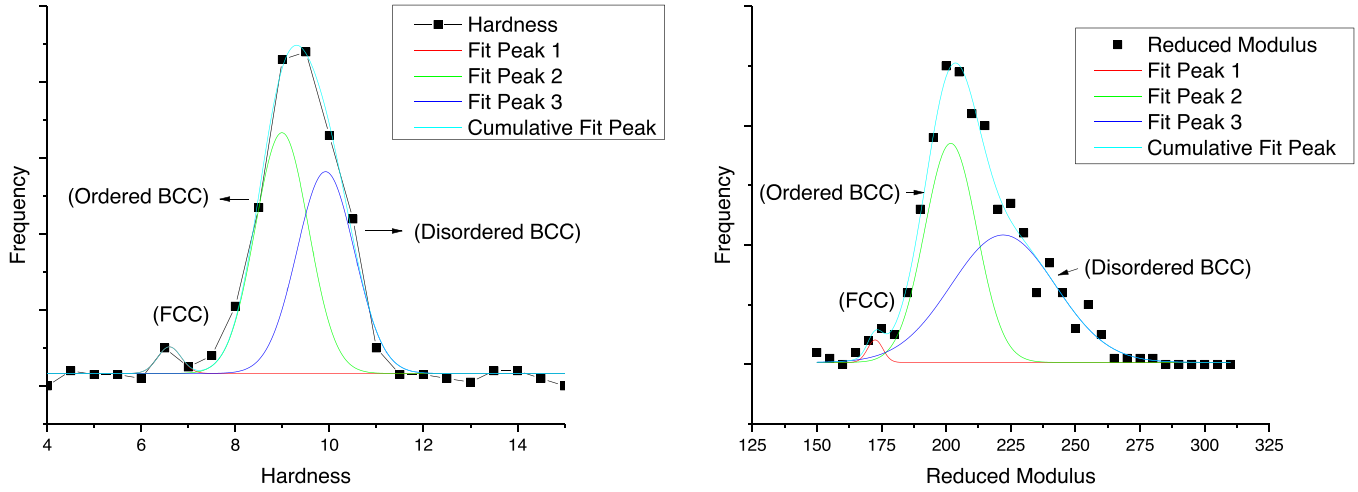

Fig. 11. Phase deconvolution of hardness and reduced modulus values extracted from nano-indentations maps and showing the results of the properties for the individual phases.

Fig. 9 shows a plot of the hardness versus e/a values of different HEAs from the literature. The majority of literature values come from the FCC+BCC domain, while the composition of this study is somewhere between domains II (FCC+BCC) and III (BCC) [38]. A single study [40] has obtained values above 10 GPa with an $Al_3CoCrCuFeNi$ composition, heavily BCC stabilized due to the high Al content, higher than the values obtained for $Al_{1.8}CoCrCu_{0.5}FeNi$ in the present work. Even though each study used different test parameters, which introduces a scattering in the hardness data, Fig. 9 shows a general trend where the hardness of BCC HEAs with large e/a values (Domain III) is higher than that of mixed FCC+BCC HEAs from Domain II. Considering that e/a values correlate to the proportion of FCC and BCC phases, our HEAs are expected to present hardness values around 8–9 GPa, consistent with the measurements obtained in Table 6 and validating the e/a approach for the hardness as well as the structure prediction. Moreover, the graphs also illustrate the hardness changes produced in the $Al_{1.8}CoCrCu_{0.5}FeNi$ alloy through different processing methods.

Contour mappings of nano-indentations were performed on the surface of the HT sample to obtain individual phase measurements. The results are shown in Fig. 10. A backscattered SEM micrograph of the same region, post-indentations, is also included to identify each measurement and phase. From the hardness contour map, various phases can be distinguished, the most clearly visible one being the blue region in the middle, which when compared to the SEM image is attributed to the softer Cu-rich phase. This softer FCC phase shows a pile-up effect in the surface surrounding the nano-indentation pit. This phenomenon has been observed by Muthupandi et al. [78] in an AlCoCrFeNi with ordered/disordered BCC phases and a FCC phase similar to those observed in the present study.The pile-up behaviour occurs due to the absence of sufficient dislocations shifting through the slip direction, parallel to the surface, h. Additionally, the activation energy for the dislocation slip is lower in FCC structures compared to BCC lattices, making pile-up more likely to happen in the former, especially at low loads.

To complete the mechanical characterisation of the individual phases, a Gauss deconvolution of the hardness and reduced modulus distribution from the data in the contour maps was also analysed and is displayed in Fig. 11. Both BCC structures show higher reduced elastic modulus and hardness than the FCC phase. In the case of the hardness, the two BCC phases vary between 8 and 10 GPa, with the ordered phase being softer than the disordered BCC. However, in the case of the reduced modulus, the difference is larger, between 200 and 225 GPa, with the disordered BCC being the highest one.

4. Conclusions

The influence on hardness and elastic modulus in an $Al_{1.8}CoCrCu_{0.5}FeNi$ HEA obtained by different processing methods was studied. It was found that the crystalline structure in the different processes does not change. However, the phase morphology evolved from cuboidal precipitates to weave-like phases.

In all the processing routes, the HEA is composed of various phases: ordered BCC (Al-rich), disordered BCC (Cr-rich) and a minor FCC (Cu-rich). Following the MA process produces a change in the morphology and refinement of grain structure, as well as the distribution of the FCC phase. The grain size decreased, while the original arrangement of both ordered/disordered BCC phases changed, along with an increase of the FCC phase up to about 5 vol%.

The different samples have been characterised mechanically by nano-indentation. The results obtained are considered in a multiscale frame, in relation to the production methods as well as the properties of the constituent phases. The results show that the MA method increased the hardness and young modulus compared to the same composition of the HEA obtained by gas atomization and subsequent SPS. The mechanical properties of the constituent phases were studied. The ordered/disordered BCC phases show slight differences in hardness values but larger differences in the elastic modulus. Several strengthening mechanisms were evaluated and discussed from the reported literature, to observe their influence on the mechanical properties from the unique combination of a BCC-HEA and the MA approach. The grain size reduction, the increased dislocation density and the precipitation hardening have been shown to be the main contributors to the increase in hardness and elastic modulus. The consequences of this study open up new possibilities in the future development of the HEA that show ordered/disordered BCCs structures.

CRediT authorship contribution statement

Eduardo Reverte: Formal analysis, Investigation, Methodology, Validation, Writing – original draft. **Clement Keller:** Methodology, Investigation, Validation, Writing – review & editing. **Monique Calvo-Dahlborg:** Investigation, Validation, Writing – review & editing. **German Alcalá:** Methodology, Investigation, Validation, Writing – review & editing. **Monica Campos:** Methodology, Investigation, Supervision, Validation, Writing – review & editing, Funding acquisition. **Juan Cornide:** Conceptualization, Formal analysis, Funding acquisition, Investigation, Methodology, Supervision, Validation, Writing – review & editing.

Data Availability

No data was used for the research described in the article.

Declaration of Competing Interest

The authors declare that they have no known competing financial interests or personal relationships that could have appeared to influence the work reported in this paper.

Acknowledgements

This research was supported by the Regional Government of Madrid under the programme S2018/NMT-4381-MAT4.0-CM project. Funding from PID2019–109334RB-C32 awarded by the Spanish Ministry of Science, Innovation and Universities is also acknowledged. J. Cornide also acknowledges funding from the Spanish Ministry of Science and Innovation (IJCI-2017–31348) and TED2021–130831B-I00 funded by MCIN/AEI/10.13039/501100011033 and NextGenerationEU/PRTR. Funding for APC: Universidad Carlos III de Madrid (Read & Publish Agreement CRUE-CSIC 2023).

References

[1] B. Cantor, I.T.H. Chang, P. Knight, A.J.B. Vincent, Microstructural development in equiatomic multicomponent alloys, Mater. Sci. Eng. A 375–377 (2004) 213–218, https://doi.org/10.1016/J.MSEA.2003.10.257
[2] J.W. Yeh, S.-K. Chen, S.-J. Lin, J.-Y. Gan, T.-S. Chin, T.-T. Shun, C.-H. Tsau, S.-Y. Chang, Nanostructured high-entropy alloys with multiple principal elements: Novel alloy design concepts and utcomes, Adv. Eng. Mater. 6 (2004) 299–303, https://doi.org/10.1002/adem.200300567
[3] M.C. Gao, P.K. Liaw, J.W. Yeh, Y. Zhang, High-entropy alloys: fundamentals and applications, high-entropy alloy, Fundam. Appl. (2016) 1–516, https://doi.org/10.1007/978-3-319-27013-5
[4] S. Guo, Q. Hu, C. Ng, C.T. Liu, More than entropy in high-entropy alloys: forming solid solutions or amorphous phase, Intermetallics 41 (2013) 96–103, https://doi.org/10.1016/J.INTERMET.2013.05.002
[5] W. Steurer, Single-phase high-entropy alloys – a critical update, Mater. Charact. 162 (2020) 110179, https://doi.org/10.1016/J.MATCHAR.2020.110179
[6] D.J.M. King, S.C. Middleburgh, A.G. McGregor, M.B. Cortie, Predicting the formation and stability of single phase high-entropy alloys, Acta Mater. 104 (2016) 172–179, https://doi.org/10.1016/J.ACTAMAT.2015.11.040
[7] U. Dahlborg, J. Cornide, M. Calvo-Dahlborg, T.C. Hansen, A. Fitch, Z. Leong, S. Chambreland, R. Goodall, Structure of some CoCrFeNi and CoCrFeNiPd multicomponent HEA alloys by diffraction techniques, J. Alloy. Compd. 681 (2016) 330–341, https://doi.org/10.1016/j.jallcom.2016.04.248
[8] M.-H. Tsai, K.-C. Chang, J.-H. Li, R.-C. Tsai, A.-H. Cheng, A second criterion for sigma phase formation in high-entropy alloys, Mater. Res. Lett. 4 (2016) 90–95, https://doi.org/10.1080/21663831.2015.1121168
[9] C.J. Tong, M.R. Chen, S.K. Chen, J.W. Yeh, T.T. Shun, S.J. Lin, S.Y. Chang, Mechanical performance of the AlxCoCrCuFeNi high-entropy alloy system with multiprincipal elements, Metall. Mater. Trans. A Phys. Metall. Mater. Sci., Miner., Met. Mater. Soc. (2005) 1263–1271, https://doi.org/10.1007/s11661-005-0218-9
[10] M.R. Chen, S.J. Lin, J.W. Yeh, S.K. Chen, Y.S. Huang, M.H. Chuang, Effect of vanadium addition on the microstructure, hardness, and wear resistance of Al0.5CoCrCuFeNi high-entropy alloy, Metall. Mater. Trans. A 375 (37) (2006) 1363–1369, https://doi.org/10.1007/S11661-006-0081-3
[11] C. Li, J.C. Li, M. Zhao, L. Zhang, Q. Jiang, Microstructure and properties of AlTiNiMnBx high entropy alloys, Http://Dx.Doi.Org/10.1179/174328408×275964. 24 (2013) 376–378. https://doi.org/10.1179/174328408×275964.
[12] Y.F. Kao, T.J. Chen, S.K. Chen, J.W. Yeh, Microstructure and mechanical property of as-cast, -homogenized, and -deformed AlxCoCrFeNi (0 ≤ x ≤ 2) high-entropy alloys, J. Alloy. Compd. 488 (2009) 57–64, https://doi.org/10.1016/J.JALLCOM.2009.08.090
[13] S.T. Chen, W.Y. Tang, Y.F. Kuo, S.Y. Chen, C.H. Tsau, T.T. Shun, J.W. Yeh, Microstructure and properties of age-hardenable AlxCrFe1.5MnNi0.5 alloys, Mater. Sci. Eng. A 527 (2010) 5818–5825, https://doi.org/10.1016/J.MSEA.2010.05.052
[14] O.N. Senkov, C.F. Woodward, Microstructure and properties of a refractory NbCrMo0.5Ta0.5TiZr alloy, Mater. Sci. Eng. A 529 (2011) 311–320, https://doi.org/10.1016/J.MSEA.2011.09.033
[15] O.N. Senkov, S.V. Senkova, C. Woodward, Effect of aluminum on the microstructure and properties of two refractory high-entropy alloys, Acta Mater. 68 (2014) 214–228, https://doi.org/10.1016/J.ACTAMAT.2014.01.029
[16] A.V. Kuznetsov, D.G. Shaysultanov, N.D. Stepanov, G.A. Salishchev, O.N. Senkov, Tensile properties of an AlCrCuNiFeCo high-entropy alloy in as-cast and wrought conditions, Mater. Sci. Eng. A 533 (2012) 107–118, https://doi.org/10.1016/J.MSEA.2011.11.045
[17] A. Gali, E.P. George, Tensile properties of high- and medium-entropy alloys, Intermetallics 39 (2013) 74–78, https://doi.org/10.1016/J.INTERMET.2013.03.018
[18] Z. Tang, T. Yuan, C.W. Tsai, J.W. Yeh, C.D. Lundin, P.K. Liaw, Fatigue behavior of a wrought Al0.5CoCrCuFeNi two-phase high-entropy alloy, Acta Mater. 99 (2015) 247–258, https://doi.org/10.1016/J.ACTAMAT.2015.07.004
[19] M.A. Hemphill, T. Yuan, G.Y. Wang, J.W. Yeh, C.W. Tsai, A. Chuang, P.K. Liaw, Fatigue behavior of Al0.5CoCrCuFeNi high entropy alloys, Acta Mater. 60 (2012) 5723–5734, https://doi.org/10.1016/J.ACTAMAT.2012.06.046
[20] M. Seifi, D. Li, Z. Yong, P.K. Liaw, J.J. Lewandowski, Fracture toughness and fatigue crack growth behavior of as-cast high-entropy alloys, JOM 67 (2015) 2288–2295, https://doi.org/10.1007/S11837-015-1563-9
[21] B. Gludovatz, A. Hohenwarter, D. Catoor, E.H. Chang, E.P. George, R.O. Ritchie, A fracture-resistant high-entropy alloy for cryogenic applications, Science 345 (80) (2014) 1153–1158, https://doi.org/10.1126/science.1254581
[22] J.M. Wu, S.J. Lin, J.W. Yeh, S.K. Chen, Y.S. Huang, H.C. Chen, Adhesive wear behavior of AlxCoCrCuFeNi high-entropy alloys as a function of aluminum content, Wear 261 (2006) 513–519, https://doi.org/10.1016/j.wear.2005.12.008
[23] X.W. Qiu, Microstructure and properties of AlCrFeNiCoCu high entropy alloy prepared by powder metallurgy, J. Alloy. Compd. 555 (2013) 246–249, https://doi.org/10.1016/j.jallcom.2012.12.071
[24] Y.J. Chang, A.C. Yeh, The evolution of microstructures and high temperature properties of AlxCo1.5CrFeNi1.5Tiy high entropy alloys, J. Alloy. Compd. 653 (2015) 379–385, https://doi.org/10.1016/J.JALLCOM.2015.09.042
[25] O.N. Senkov, G.B. Wilks, D.B. Miracle, C.P. Chuang, P.K. Liaw, Refractory high-entropy alloys, Intermetallics 18 (2010) 1758–1765, https://doi.org/10.1016/j.intermet.2010.05.014
[26] O.N. Senkov, G.B. Wilks, J.M. Scott, D.B. Miracle, Mechanical properties of Nb25Mo25Ta25W25 and V20Nb20Mo20Ta20W20 refractory high entropy alloys, Intermetallics 19 (2011) 698–706, https://doi.org/10.1016/J.INTERMET.2011.01.004
[27] H.W. Yao, J.W. Qiao, M.C. Gao, J.A. Hawk, S.G. Ma, H.F. Zhou, Y. Zhang, NbTaV-(Ti,W) refractory high-entropy alloys: experiments and modeling, Mater. Sci. Eng. A 674 (2016) 203–211, https://doi.org/10.1016/J.MSEA.2016.07.102
[28] H. Yao, J.W. Qiao, M.C. Gao, J.A. Hawk, S.G. Ma, H. Zhou, MoNbTaV medium-entropy alloy, Entropy Vol. 18 (2016) 189, https://doi.org/10.3390/E18050189
[29] I. Toda-Caraballo, P.E.J. Rivera-Díaz-del-Castillo, A criterion for the formation of high entropy alloys based on lattice distortion, Intermetallics 71 (2016) 76–87, https://doi.org/10.1016/J.INTERMET.2015.12.011
[30] Z. Wang, W. Qiu, Y. Yang, C.T. Liu, Atomic-size and lattice-distortion effects in newly developed high-entropy alloys with multiple principal elements, Intermetallics 64 (2015) 63–69, https://doi.org/10.1016/J.INTERMET.2015.04.014
[31] M.C. Troparevsky, J.R. Morris, P.R.C. Kent, A.R. Lupini, G.M. Stocks, Criteria for predicting the formation of single-phase high-entropy alloys, Phys. Rev. X 5 (2015) 011041, https://doi.org/10.1103/PHYSREVX.5.011041/FIGURES/2/MEDIUM
[32] M.G. Poletti, L. Battezzati, Electronic and thermodynamic criteria for the occurrence of high entropy alloys in metallic systems, Acta Mater. 75 (2014) 297–306, https://doi.org/10.1016/j.actamat.2014.04.033
[33] Y. Lu, Y. Dong, L. Jiang, T. Wang, T. Li, Y. Zhang, A criterion for topological close-packed phase formation in high entropy alloys, Entropy Vol. 17 (2015) 2355–2366, https://doi.org/10.3390/E17042355
[34] Z. Leong, J.S. Wróbel, S.L. Dudarev, R. Goodall, I. Todd, D. Nguyen-Manh, The effect of electronic structure on the phases present in high entropy alloys, Sci. Rep. 7 (2017) 39803, https://doi.org/10.1038/srep39803
[35] Effect of Electron Density on Phase Composition of High-Entropy Equiatomic Alloys | SpringerLink, (n.d.). https://link.springer.com/article/10.1007/s11106–016-9754–7 (accessed September 26, 2022).
[36] F. Tancret, I. Toda-Caraballo, E. Menou, P.E.J.Rivera Díaz-Del-Castillo, Designing high entropy alloys employing thermodynamics and Gaussian process statistical analysis, Mater. Des. 115 (2017) 486–497, https://doi.org/10.1016/J.MATDES.2016.11.049
[37] M. Calvo-Dahlborg, S.G.R. Brown, Hume-Rothery for HEA classification and self-organizing map for phases and properties prediction, J. Alloy. Compd. 724 (2017) 353–364, https://doi.org/10.1016/J.JALLCOM.2017.07.074
[38] M. Calvo-Dahlborg, U. Dahlborg, S.G.R. Brown, J. Juraszek, Influence of the electronic polymorphism of Ni on the classification and design of high entropy alloys, J. Alloy. Compd. 824 (2020), https://doi.org/10.1016/j.jallcom.2020.153895
[39] M. Calvo-Dahlborg, S. Mehraban, N.P. Lavery, S.G.R. Brown, J. Cornide, J. Cullen, J. Cieslak, Z. Leong, R. Goodall, U. Dahlborg, Prediction of phase, hardness and density of high entropy alloys based on their electronic structure and average radius, J. Alloy. Compd. 865 (2021) 158799, https://doi.org/10.1016/j.jallcom.2021.158799
[40] Y. Sun, P. Chen, L. Liu, M. Yan, X. Wu, C. Yu, Z. Liu, Local mechanical properties of AlxCoCrCuFeNi high entropy alloy characterized using nanoindentation, Intermetallics 93 (2018) 85–88, https://doi.org/10.1016/J.INTERMET.2017.11.010
[41] K. Matusiak, K. Berent, M. Marciszko, J. Cieslak, The experimental and theoretical study on influence of Al and Cu contents on phase abundance changes in AlxCuyFeCrNiCo HEA system, J. Alloy. Compd. 790 (2019) 837–846, https://doi.org/10.1016/J.JALLCOM.2019.03.162
[42] C.D. Gómez-Esparza, R.A. Ochoa-Gamboa, I. Estrada-Guel, J.G. Cabañas-Moreno, J.I. Barajas-Villarruel, A. Arizmendi-Morquecho, J.M. Herrera-Ramírez, R. Martínez-Sánchez, Microstructure of NiCoAlFeCuCr multi-component systems synthesized by mechanical alloying, J. Alloy. Compd. 509 (2011) S279–S283, https://doi.org/10.1016/j.jallcom.2010.12.105
[43] E. Reverte, J. Cornide, M.A. Lagos, M. Campos, P. Alvaredo, Microstructure evolution in a fast and ultrafast sintered non-equiatomic Al/Cu HEA, Met. (Basel) 11 (2021), https://doi.org/10.3390/met11060848

[44] E. Reverte, M. Calvo-Dahlborg, U. Dahlborg, M. Campos, P. Alvaredo, P. Martin-Rodriguez, E. Gordo, J. Cornide, Design and production of a new FeCoNiCrAlCu high-entropy alloy: influence of powder production method on sintering, Mater. (Basel) 14 (2021), https://doi.org/10.3390/ma14154342
[45] J.M. Torralba, P. Alvaredo, A. García-Junceda, High-entropy alloys fabricated via powder metallurgy. A critical review, Powder Met. 62 (2019) 84–114, https://doi.org/10.1080/00325899.2019.1584454
[46] E. Colombini, M. Lassinantti Gualtieri, R. Rosa, F. Tarterini, M. Zadra, A. Casagrande, P. Veronesi, SPS-assisted Synthesis of SICp reinforced high entropy alloys: reactivity of SIC and effects of pre-mechanical alloying and post-annealing treatment, Https://Doi.Org/10.1080/00325899.2017.1393162. 61 (2017) 64–72. https://doi.org/10.1080/00325899.2017.1393162.
[47] Ł. Rogal, D. Kalita, A. Tarasek, P. Bobrowski, F. Czerwinski, Effect of SiC nanoparticles on microstructure and mechanical properties of the CoCrFeMnNi high entropy alloy, J. Alloy. Compd. 708 (2017) 344–352, https://doi.org/10.1016/J.JALLCOM.2017.02.274
[48] K. Raja Rao, S.K. Sinha, Strengthening of AlCoCrFeNi based high entropy alloy with nano- Y2O3 dispersion, 281 (2022) 115720, https://doi.org/10.1016/J.MSEB.2022.115720
[49] Y. Ma, B. Jiang, C. Li, Q.B. morphologies in A. high-entropy alloys Wang, C. Dong, P.K. Liaw, F. Xu, L. Sun, The BCC/B2 Morphologies in AlxNiCoFeCr High-Entropy Alloys, Metals (Basel). 7 (2017). https://doi.org/10.3390/met7020057.
[50] J.L. Li, Z. Li, Q. Wang, C. Dong, P.K. Liaw, Phase-field simulation of coherent BCC/B2 microstructures in high entropy alloys, Acta Mater. 197 (2020) 10–19, https://doi.org/10.1016/j.actamat.2020.07.030
[51] C.J. Tong, Y.L. Chen, S.K. Chen, J.W. Yeh, T.T. Shun, C.H. Tsau, S.J. Lin, S.Y. Chang, Microstructure characterization of AlxCoCrCuFeNi high-entropy alloy system with multiprincipal elements, Metall. Mater. Trans. A Phys. Metall. Mater. Sci. 36 (2005) 881–893, https://doi.org/10.1007/s11661-005-0283-0
[52] I. Moravcik, A. Kubicek, L. Moravcikova-Gouvea, O. Adam, V. Kana, V. Pouchly, A. Zadera, I. Dlouhy, The origins of high-entropy alloy contamination induced by mechanical alloying and sintering, Met Vol. 10 (2020) 1186, https://doi.org/10.3390/MET10091186
[53] V.S. Vinila, J. Isac, Synthesis and structural studies of superconducting perovskite GdBa2Ca3Cu4O10.5+δ nanosystems, Des. Fabr. Charact. Multifunct. Nanomater (2022) 319–341, https://doi.org/10.1016/B978-0-12-820558-7.00022-4
[54] C. Suryanarayana, Mechanical alloying and milling, Prog. Mater. Sci. 46 (2001) 1–184, https://doi.org/10.1016/S0079-6425(99)00010-9
[55] W. Schatt, K.-P. Wieters, European Powder Metallurgy Association., Powder metallurgy: processing and materials, (1997) 492. https://books.google.com/books/about/Powder_Metallurgy.html?hl=es&id=LpLgAAAAMAAJ (accessed October 17, 2022).
[56] J. Eckert, J.C. Holzer, C.E. Krill, W.L. Johnson, Structural and thermodynamic properties of nanocrystalline fcc metals prepared by mechanical attrition, J. Mater. Res. 7 (1992) 1751–1761, https://doi.org/10.1557/JMR.1992.1751/METRICS
[57] S. Ohtsuka, S. Ukai, M. Fujiwara, T. Kaito, T. Narita, Nano-structure control in ODS martensitic steels by means of selecting titanium and oxygen contents, J. Phys. Chem. Solids, Pergamon, 2005, pp. 571–575, https://doi.org/10.1016/j.jpcs.2004.06.033
[58] S. Ohtsuka, S. Ukai, M. Fujiwara, T. Kaito, T. Narita, Improvement of 9Cr-ODS martensitic steel properties by controlling excess oxygen and titanium contents, in: J. Nucl. Mater., North-Holland, 2004: pp. 372–376. https://doi.org/10.1016/j.jnucmat.2004.04.043.
[59] P. Olier, J. Malaplate, M.H. Mathon, D. Nunes, D. Hamon, L. Toualbi, Y. De Carlan, L. Chaffron, Chemical and microstructural evolution on ODS Fe–14CrWTi steel during manufacturing stages, J. Nucl. Mater. 428 (2012) 40–46, https://doi.org/10.1016/J.JNUCMAT.2011.10.042
[60] M. Ogura, T. Fukushima, R. Zeller, P.H. Dederichs, Structure of the high-entropy alloy AlxCrFeCoNi: Fcc versus bcc, J. Alloy. Compd. 715 (2017) 454–459, https://doi.org/10.1016/j.jallcom.2017.04.318
[61] M. Li, J. Gazquez, A. Borisevich, R. Mishra, K.M. Flores, Evaluation of microstructure and mechanical property variations in AlxCoCrFeNi high entropy alloys produced by a high-throughput laser deposition method, Intermetallics 95 (2018) 110–118, https://doi.org/10.1016/J.INTERMET.2018.01.021
[62] A.F. Andreoli, X. Han, I. Kaban, In situ studies of non-equilibrium crystallization of AlxCoCrFeNi (x = 0.3, 1) high-entropy alloys, J. Alloy. Compd. 922 (2022) 166209, https://doi.org/10.1016/J.JALLCOM.2022.166209
[63] L. Yu, Z. Lu, S. Peng, X. Li, Effect of Al/Ti ratio on γ′ and oxide dispersion strengthening in Ni-based ODS superalloys, Mater. Sci. Eng. A. 845 (2022) 143240, https://doi.org/10.1016/J.MSEA.2022.143240
[64] C. Keller, K. Tabalaiev, G. Marnier, J. Noudem, X. Sauvage, E. Hug, Influence of spark plasma sintering conditions on the sintering and functional properties of an ultra-fine grained 316L stainless steel obtained from ball-milled powder, Mater. Sci. Eng. A 665 (2016) 125–134, https://doi.org/10.1016/J.MSEA.2016.04.039
[65] R.S. Ganji, P. Sai Karthik, K. Bhanu Sankara Rao, K.V. Rajulapati, Strengthening mechanisms in equiatomic ultrafine grained AlCoCrCuFeNi high-entropy alloy studied by micro- and nanoindentation methods, Acta Mater. 125 (2017) 58–68, https://doi.org/10.1016/j.actamat.2016.11.046
[66] R. Sriharitha, B.S. Murty, R.S. Kottada, Alloying, thermal stability and strengthening in spark plasma sintered AlxCoCrCuFeNi high entropy alloys, J. Alloy. Compd. 583 (2014) 419–426, https://doi.org/10.1016/j.jallcom.2013.08.176
[67] S. Peng, J. Hou, L. Yu, Z. Lu, Effects of sintering temperature and Y2O3/Ti addition on microstructure and hardness of ODS-AlCrFeNi HEAs, Intermetallics 143 (2022), https://doi.org/10.1016/J.INTERMET.2022.107469
[68] W.H. Liu, Y. Wu, J.Y. He, T.G. Nieh, Z.P. Lu, Grain growth and the Hall–Petch relationship in a high-entropy FeCrNiCoMn alloy, Scr. Mater. 68 (2013) 526–529, https://doi.org/10.1016/J.SCRIPTAMAT.2012.12.002
[69] P. Edalati, A. Mohammadi, M. Ketabchi, K. Edalati, Microstructure and microhardness of dual-phase high-entropy alloy by high-pressure torsion: twins and stacking faults in FCC and dislocations in BCC, J. Alloy. Compd. 894 (2022) 162413, https://doi.org/10.1016/J.JALLCOM.2021.162413
[70] R. Labusch, Statistische theorien der mischkristallhärtung, Acta Met. 20 (1972) 917–927, https://doi.org/10.1016/0001-6160(72)90085-5
[71] N.F.Mott , CXVII . A theory of work-hardening of metal crystals, http://Dx.Doi.Org/10.1080/14786441108521024. 43 (2010) 1151–1178. https://doi.org/10.1080/14786441108521024.
[72] R. Labusch, A statistical theory of solid solution hardening, Phys. Status Solidi 41 (1970) 659–669, https://doi.org/10.1002/PSSB.19700410221
[73] C.R. LaRosa, M. Shih, C. Varvenne, M. Ghazisaeidi, Solid solution strengthening theories of high-entropy alloys, Mater. Charact. 151 (2019) 310–317, https://doi.org/10.1016/J.MATCHAR.2019.02.034
[74] C. Baruffi, F. Maresca, W.A. Curtin, Screw vs. edge dislocation strengthening in body-centered-cubic high entropy alloys and implications for guided alloy design, MRS Commun. 12 (2022) 1111–1118, https://doi.org/10.1557/S43579-022-00278-2/FIGURES/3
[75] F.G. Coury, M. Kaufman, A.J. Clarke, Solid-solution strengthening in refractory high entropy alloys, Acta Mater. 175 (2019) 66–81, https://doi.org/10.1016/J.ACTAMAT.2019.06.006
[76] F.G. Coury, P. Wilson, K.D. Clarke, M.J. Kaufman, A.J. Clarke, High-throughput solid solution strengthening characterization in high entropy alloys, Acta Mater. 167 (2019) 1–11, https://doi.org/10.1016/J.ACTAMAT.2019.01.029
[77] P.C. Carnavas, N.W. Page, Elastic properties of compacted metal powders, J. Mater. Sci. 33 (1998) 4647–4655, https://doi.org/10.1023/A:1004445527430/METRICS
[78] G. Muthupandi, K.R. Lim, Y.S. Na, J. Park, D. Lee, H. Kim, S. Park, Y.S. Choi, Pile-up and sink-in nanoindentation behaviors in AlCoCrFeNi multi-phase high entropy alloy, Mater. Sci. Eng. A 696 (2017) 146–154, https://doi.org/10.1016/J.MSEA.2017.04.045